

ORIGINAL RESEARCH

Design procedure and optimisation methodology of permanent magnet synchronous machines with direct slot cooling for aviation electrification

Ahmed Tameemi¹  | Michele Degano² | Mukhammed Murataliyev² |
Mauro Di Nardo²  | Giorgio Valente^{2,3} | David Gerada² | Zeyuan Xu² | Chris Gerada²

¹Department of Communication Technical Engineering, Al-Farahidi University, Baghdad, Iraq

²Department of Electrical and Electronic Engineering, University of Nottingham, University Park, Nottingham, UK

³Applied Solutions Group, Part of Hexagon Manufacturing Intelligence, Nottingham, UK

Correspondence

Ahmed Tameemi, Department of Communication Technical Engineering, Al-Farahidi University, Baghdad, Iraq.
Email: Ahmed.altimimy@uofarahidi.edu.iq

Abstract

Electric machines are widely employed in a variety of sectors, including automotive and aerospace industry. With the rising trend towards electrification in aviation, electric machines with increased power density and efficiency are becoming key enabling technologies, requiring the development of innovative design procedures. In this study, a preliminary design procedure for Surface Mounted Permanent Magnet Synchronous Machines (SPMSMs) intensively cooled by means of oil channels placed in the stator slots is proposed. The analytical derivation of SPMSM sizing equations, including the sub-domain model and optimisation algorithm will be reported in detail. Indeed, both the electromagnetic and thermal equations of the machine are considered for the derivation of the sizing tool. As a result, the latter allows to capture variation of the machine design not only in terms of mechanical demands, such as power and speed, but also in terms of coolant characteristics, and can be effectively employed to perform trade-off studies at a preliminary design stage. The proposed design tool will be used for a specific case study: The design of a high-speed machine for an aerospace hydraulic actuator. The accuracy of the proposed design tool is validated for different parameters by comparing the results to experimental measurements performed on an existing 8-pole 9-slot prototype SPMSM.

KEYWORDS

design, electric actuators, finite element analysis, optimisation, permanent magnet machines

1 | INTRODUCTION

Nowadays, the commercial aviation industry is experiencing a significant expansion as the air traffic has been growing in the last decades, and it is predicted to double in the next 15 years [1]. This trend will lead to a dramatic increase in fuel consumption and CO₂ emissions [2]. For these reasons, increasingly strict regulations are encouraging the aircraft industries to move towards the use of electrical actuator systems (e.g., with the so called More Electric Aircraft initiative) [3] or hybrid or fully electric propulsion system [4]. Indeed, electrical hydraulic actuators (EHAs) and/or electronic mechanical actuators (EMAs) lead to more efficient, reliable, and environmentally friendly

operations if compared to conventional ones [3]. This is of great significance for aerospace applications where high-performance actuation systems must satisfy strict safety and reliability standards along with efficiency and weight targets [5, 6]. The electric hydraulic actuators (EHAs) are indeed a favourite solution for hydraulic systems, particularly for applications with integrated motors and pumps [7]. With this kind of embedded actuators, the hydraulic pump is driven at a variable speed by an electric motor to transfer the hydraulic fluid [5]. The lack of shaft seals and the possible enhancement of the machine's thermal rating are the primary advantages of having a motor directly connected to the pump [8, 9]. Recently, there has been a growing interest in electrical machines with high performance direct

This is an open access article under the terms of the Creative Commons Attribution License, which permits use, distribution and reproduction in any medium, provided the original work is properly cited.

© 2022 The Authors. *IET Electric Power Applications* published by John Wiley & Sons Ltd on behalf of The Institution of Engineering and Technology.

liquid cooling systems such as the one featuring cooling channels in the stator slots [10]. Even though high-power generators installed in electric power plants have employed direct cooling windings for decades [11], the same technology has not yet been applied in low-voltage, high torque, high-efficiency, and compact-size machines with high overload capacity [1]. In particular, this interest has been sparked by the growing need for high-power-density motors and generators for both aerospace and automotive applications. In Refs. [10–15] special cooling methods and the respective machine thermal management have been investigated. Indeed, it is shown how both power and current densities can be dramatically increased, by applying intensive cooling approaches.

Although the desired level of detail and accuracy can be obtained with finite element analysis (FEA), modelling the entire electrical machine by using numerical approaches, including the cooling, is a complicated and time-consuming process that requires knowledge of multiple fields of physics [16]. Consider the thermal, mechanical, and electromagnetic domains. Furthermore, when designing machines with the advanced cooling systems, for example, the stator slot cooling, more precise and detailed design methods are required [15]. The latter are crucial if the high power density of the electrical machine in such work is to be achieved, and therefore, they must be incorporated within the preliminary design. As a result, it is evident that a machine sizing tool is required for quickly generating and evaluating optimal electrical machine solutions under specified restrictions, while taking into consideration the different scenarios involved.

To bridge this gap, this paper proposes an analytical sizing approach by combining the sub-domain model to predict the electromagnetic performance [17] and a lumped parameter

thermal model to calculate the steady-state temperature of the motor. In surface-mounted PM machines (SPMs), the sub-domain analytical model makes it possible to account for the effect of stator slotting and further to calculate the open-circuit magnetic field [18].

Subsequently, the optimisation algorithm, combined with the sub-domain model and thermal model, was developed to perform the preliminary design of a high-power density SPM machine intensively cooled via oil channels placed in the stator slots. This approach relies on solving a system of two non-linear equations related to the electromagnetic and thermal limits, respectively. The advantages of this approach are that it appears to be simpler and requires less computational time.

In this work, the main objective is to describe the development of such a sizing tool. In the first part, the methodology behind the tool development and the equivalent mathematical formulations of the optimal design problem of a PM machine are described in Section 2, while Section 3 presents the complete design and optimisation process. Section 4 includes a comprehensive sensitivity analysis of machine performance as well as shows the results of the sizing tool with key parameters. Section 5 presents and compares the results of a validation of the proposed sizing tool to a previously built PMSM for an aerospace application. Finally, Section 6 reports the conclusions and findings of this work.

2 | ANALYTICAL DESIGN

The sizing tool presented in this study considers an SPM machine with oil channels in the stator slots for intense cooling, as schematically represented in Figure 1. Both distributed windings and concentrated winding topologies can be considered. A quasi-Halbach configuration is used for the rotor PM configuration which allows obtaining a high fundamental air gap flux density with a minimum harmonic content [7]. The tool assumes linear magnetic properties of the ferromagnetic materials and that all the losses produced by the stator windings are dissipated through the oil channels in the slots. By using the proposed design tool, machine size may be captured as a function of mechanical requirements (such as power and speed) as well as coolant characteristics. The electrical machine is designed with a single operating point, which corresponds to the specified output power and rotational speed.

The stack length over the stator's inner diameter (i.e., aspect ratio L_{stk}/D_{si}) and cooling channel area are also considered variables during the design procedure. Indeed, the aspect ratio affects not only the machine size and weight but also the rotor peripheral speed, hence the rotor mechanical stresses, and can be used to optimise the design.

A system of two non-linear equations must be solved as it is described in Equation (1) to identify two critical machine parameters: the stator inner diameter D_{si} and the machine's electrical loading K_s . These are used to calculate all the main machine dimensions once the system of Equation (1) is solved.

$$\begin{cases} \text{equation 1} \\ \text{equation 2} \end{cases} = \begin{cases} D_{si} \\ K_s \end{cases} \quad (1)$$

where *equation 1* represents the electromagnetic torque equation of the SPM machine and *equation 2* is the equation of the thermal balance in the slot.

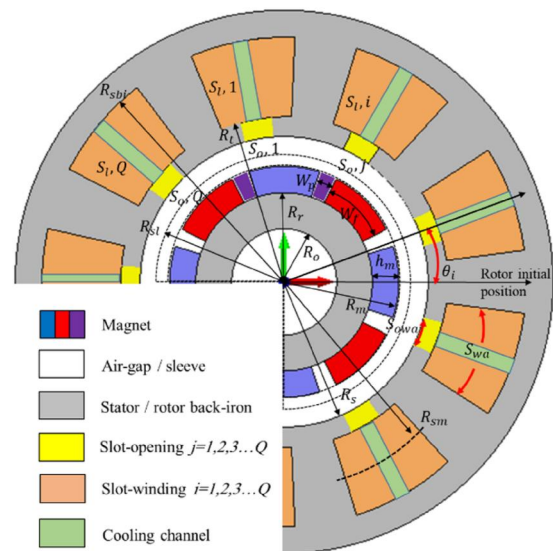


FIGURE 1 Cross section of the SPM machine.

In the next two sub-sections the electromagnetic and thermal analysis required to derive *equation 1* and *equation 2* are described.

2.1 | Sub-domain electromagnetic model

The first part of the SPM design consists of computing the air gap flux density B_g . An analytical sub-domain model (SD) is adopted in this study for the air gap magnetic field calculation that takes the stator slotting effect into account.

In order to simplify the problem, a few assumptions are applied: infinite permeability in the stator and rotor cores, no electrical conductivity in the rotor and stator laminations, uniform distributed current density in the slot area, end-effects are neglected in this model, and the permanent magnet have a liner demagnetisation characteristics [17, 19].

2.1.1 | Model of the PMs

For a 2D problem in polar coordinates, the magnetisation vector of the permanent magnet is expressed by its radial and tangential components as in Ref. [20].

$$\vec{M} = M_r \vec{r} + M_\theta \vec{\theta} \quad (8)$$

where M_r and M_θ are the radial and tangential components of the magnetisation vector. \vec{r} and $\vec{\theta}$ are the radial and tangential unit vectors, respectively. For both radial and tangential components, M_r and M_θ can be expressed as a Fourier series that is,

$$M_r = \sum_{k=1, 3, 5, \dots}^{\infty} M_{rk} \cos(kp\theta - kp\omega_r t - kp\theta_0) \quad (9)$$

$$= \sum_{k=1, 3, 5, \dots}^{\infty} M_{rck} \cos kp\theta + M_{rsk} \sin kp\theta \quad (10)$$

$$M_\theta = \sum_{k=1, 3, 5, \dots}^{\infty} M_{\theta k} \sin(kp\theta - kp\omega_r t - kp\theta_0) \quad (11)$$

$$= \sum_{k=1, 3, 5, \dots}^{\infty} M_{\theta ck} \cos kp\theta + M_{\theta sk} \sin kp\theta \quad (12)$$

$$M_{rck} = M_{rk} \cos(kp\omega_r t + kp\theta_0) \quad (13)$$

$$M_{rsk} = M_{rk} \sin(kp\omega_r t + kp\theta_0) \quad (14)$$

$$M_{\theta ck} = -M_{\theta k} \sin(kp\omega_r t + kp\theta_0) \quad (15)$$

$$M_{\theta sk} = M_{\theta k} \cos(kp\omega_r t + kp\theta_0) \quad (16)$$

For a quasi-Halbach configuration with parallel magnetisation:

$$\begin{aligned} M_{rk} = \frac{B_r}{\mu_o} & \left\{ \frac{\sin \left[(1 - kp) \alpha_m \frac{\pi}{2p} \right]}{(1 - kp) \frac{\pi}{2p}} + \frac{\sin \left[(1 + kp) \alpha_m \frac{\pi}{2p} \right]}{(1 + kp) \frac{\pi}{2p}} \right\} \\ & + \frac{2B_r}{\mu_o} \left\{ \frac{\cos \left[(1 - kp) \left(\frac{\pi}{p} - \frac{\alpha_p \pi}{2p} \right) - \frac{\pi}{2p} \right]}{2(1 - kp) \frac{\pi}{p}} - \frac{\cos \left[\left(\frac{\alpha_m \pi}{2p} - \frac{kp \alpha_m \pi}{2p} \right) - \frac{\pi}{2p} \right]}{2(1 - kp) \frac{\pi}{p}} \right\} \\ & + \frac{2B_r}{\mu_o} \left\{ \frac{\cos \left[(1 + kp) \left(\frac{\pi}{p} - \frac{\alpha_p \pi}{2p} \right) - \frac{\pi}{2p} \right]}{2(1 + kp) \frac{\pi}{p}} - \frac{\cos \left[\left(\frac{\alpha_m \pi}{2p} + \frac{kp \alpha_m \pi}{2p} \right) - \frac{\pi}{2p} \right]}{2(1 + kp) \frac{\pi}{p}} \right\} \end{aligned} \quad (17)$$

$$\begin{aligned} M_{\theta k} = \frac{B_r}{\mu_o} & \left\{ \frac{-\sin \left[(1 - kp) \alpha_m \frac{\pi}{2p} \right]}{(1 - kp) \frac{\pi}{2p}} + \frac{\sin \left[(1 + kp) \alpha_m \frac{\pi}{2p} \right]}{(1 + kp) \frac{\pi}{2p}} \right\} \\ & + \frac{2B_r}{\mu_o} \left\{ \frac{\cos \left[(1 - kp) \left(\frac{\pi}{p} - \frac{\alpha_p \pi}{2p} \right) - \frac{\pi}{2p} \right]}{2(1 - kp) \frac{\pi}{p}} - \frac{\cos \left[\left(\frac{\alpha_m \pi}{2p} - \frac{kp \alpha_m \pi}{2p} \right) - \frac{\pi}{2p} \right]}{2(1 - kp) \frac{\pi}{p}} \right\} \\ & + \frac{2B_r}{\mu_o} \left\{ \frac{\cos \left[(1 + kp) \left(\frac{\pi}{p} - \frac{\alpha_p \pi}{2p} \right) - \frac{\pi}{2p} \right]}{2(1 + kp) \frac{\pi}{p}} + \frac{\cos \left[\left(\frac{\alpha_m \pi}{2p} + \frac{kp \alpha_m \pi}{2p} \right) - \frac{\pi}{2p} \right]}{2(1 + kp) \frac{\pi}{p}} \right\} \end{aligned} \quad (18)$$

where M_{rk} and $M_{\theta k}$ are respectively the k th element of the radial and tangential components of the magnetisation vector. B_r is the permanent magnet remanence, μ_o is the free space permeability, and p is the pole pairs, For the quasi-Halbach configuration, the magnet ratio α_m is defined as the ratio of the pole arc magnet with radial or parallel magnetization W_f to the transition arc magnet W_p [20].

2.1.2 | General solution of vector potential distribution

To describe the magnetic flux density, the general solutions of the vector potential for different subdomain regions can be obtained by solving the Laplace equations for the air gap and slot opening regions, whereas Poisson's equation for the magnet and winding slot regions, as expressed in Table 1 [17–19]. By applying appropriate field governing equations with specific boundaries, the air gap magnetic flux density distribution can be precisely determined using this analytical sub-domain model. In the SPM motor modelling, there are four regions, namely permanent magnet (Region 1), air-gap (Region 2), winding slot (Region $3i$, $i = 1, 2, \dots, Q$), and slot opening (Region $4j$, $j = 1, 2, \dots, Q$) as shown in Figure 1. The main parameters of this geometry are the number of stator slots Q , the stator bore radius R_{sbi} , the slot bottom radius R_b , the stator inner radius R_s , the magnet radius R_m , the rotor radius R_r , the shaft radius R_o , and the magnet pole arc to the pole pitch ratio α_p .

$A_1, B_1, C_1, D_1, A_2, B_2, C_2, D_2, C_{3i}, D_{3i}, Q_{3bi}, Q_{3ti}, C_{4j}$, and D_{4j} are the unknown coefficients to be calculated by applying appropriate boundary and interface conditions [17, 21]. θ_0 is the rotor initial position, θ is the angular position with reference to the centre of a magnet pole, θ_i is the slot position (measured from the motor centre), S_{wa} is the slot width angle, S_{owa} is the slot opening width angle, $F_m = m\pi/S_{owa}$ ($m = 1, 2, 3, \dots$), and $E_n = n\pi/S_{wa}$ ($n = 1, 2, 3, \dots$) are the harmonics order of field distribution in the stator slot opening and stator slot. A_p is a particular solution of the Poisson equation in the PM region and can be expressed as follows:

$$A_p = \sum_k l \cos(k\theta) + t \sin(k\theta) \quad (19)$$

$$l = \begin{cases} \frac{\mu_o r (M_{\theta ck} - kM_{rsk})}{k^2 - 1} & k \neq 1 \\ -\frac{\mu_o r \ln r (M_{\theta ck} - M_{rsk})}{2} & k = 1 \end{cases} \quad (20)$$

$$t = \begin{cases} \frac{\mu_o r (kM_{rck} + M_{\theta sk})}{k^2 - 1} & k \neq 1 \\ -\frac{\mu_o r \ln r (M_{\theta sk} + M_{rck})}{2} & k = 1 \end{cases} \quad (21)$$

It is worth noting that the boundary and interface conditions are determined by the continuity of the radial component of the flux density B_r and the tangential component of the field strength H_θ [21]. For the slotted SPM machine, the radial and tangential component of the magnetic flux density in the air gap (Region 2) is obtained through the solution of the governing equation that satisfies the boundary equation and can be expressed as follows:

$$B_{2r} = \frac{1}{r} \sum_k -k \left[A_2 \left(\frac{r}{R_s} \right)^k + B_2 \left(\frac{r}{R_m} \right)^{-k} \right] \sin(k\theta) + \frac{1}{r} \sum_k k \left[C_2 \left(\frac{r}{R_s} \right)^k + D_2 \left(\frac{r}{R_m} \right)^{-k} \right] \cos(k\theta) \quad (22)$$

$$B_{2\theta} = -\sum_k k \left[\frac{A_2}{R_s} \left(\frac{r}{R_s} \right)^{k-1} - \frac{B_2}{R_m} \left(\frac{r}{R_m} \right)^{-k-1} \right] \cos(k\theta) - \sum_k k \left[\frac{C_2}{R_s} \left(\frac{r}{R_s} \right)^{k-1} - \frac{D_2}{R_m} \left(\frac{r}{R_m} \right)^{-k-1} \right] \sin(k\theta)$$

2.2 | Thermal model

As previously mentioned, the considered machine is cooled by means of oil channels placed in the slots. It is also assumed that

TABLE 1 General solution of magnetic vector potential for each sub-domain

Regions	General solution	Limits
Magnet	$A_{z1} = A_p + \sum_k \left[A_1 \left(\frac{r}{R_m} \right)^k + B_1 \left(\frac{r}{R_r} \right)^{-k} \right] \cos(k\theta) + \sum_k \left[C_1 \left(\frac{r}{R_m} \right)^k + D_1 \left(\frac{r}{R_r} \right)^{-k} \right] \sin(k\theta)$	$r \in [R_r; R_m]$ (2)
Air gap	$A_{z2} = \sum_k \left[A_2 \left(\frac{r}{R_s} \right)^k + B_2 \left(\frac{r}{R_m} \right)^{-k} \right] \cos(k\theta) + \sum_k \left[C_2 \left(\frac{r}{R_s} \right)^k + D_2 \left(\frac{r}{R_m} \right)^{-k} \right] \sin(k\theta)$	$r \in [R_m; R_s]$ (3)
Winding—slot i th (Non-overlap winding)	$A_{z3i} = \sum_n \left[C_{3i} \left(\frac{r}{R_{sbi}} \right)^{E_n} + D_{3i} \left(\frac{r}{R_i} \right)^{-E_n} \right] \cdot \cos(E_n(\theta + \frac{S_{wa}}{2} - \theta_i))$	$r \in [R_i; R_{sbi}]$ (4)
Winding—bottom slot i th (Overlap winding)	$A_{z3i} = \sum_n \left[C_{3i} \left(\frac{r}{R_{sbi}} \right)^{E_n} + D_{3i} \left(\frac{r}{R_i} \right)^{-E_n} \right] \cdot \cos(E_n(\theta + \frac{S_{wa}}{2} - \theta_i)) + Q_{3bi}$	$r \in [R_i; R_{sm}]$ (5)
Winding—top slot i th (Overlap winding)	$A_{z3i} = \sum_n \left[C_{3i} \left(\frac{r}{R_{sbi}} \right)^{E_n} + D_{3i} \left(\frac{r}{R_i} \right)^{-E_n} \right] \cdot \cos(E_n(\theta + \frac{S_{wa}}{2} - \theta_i)) + Q_{3ti}$	$r \in [R_{sm}; R_{sbi}]$ (6)
Slot—openings j th	$A_{z4j} = \sum_m \left[C_{4j} (r/R_i)^{F_m} + D_{4j} (r/R_s)^{-F_m} \right] \times \cos[(F_m(\theta + \frac{S_{wa}}{2} - \theta_i))]$	$r \in [R_s; R_i]$ (7)

all the copper losses are extracted through these oil channels. A simplified lumped parameter thermal network is employed in the following in order to correlate the joule losses and so the electrical load with the coolant temperature rises. Based on these assumptions the steady state thermal balance between the stator copper and the coolant can be written as follows:

$$\Delta t_w = t_w - t_c = (R_{th,s} + R_{th,c})P_{cu} \quad (23)$$

where $R_{th,s}$ and $R_{th,c}$ are the thermal resistances between the conductors and the cooling channel (both thermal conduction and convection) and in the coolant (only convection).

In order to express Equation (23) as a function of the different aspect ratios and cooling channel fill factor, it is convenient to introduce the following dimensionless quantity

$$k_a = \frac{\pi k_{f_cond} * (1 - k_{f_cb}) w_{s-ps}^2 h_{s-ws}}{Q} \left(1 + \frac{\pi h_{s-ws}}{Q} \right) \quad (24)$$

It is now possible to write the total copper losses as

$$P_{cu} = \frac{\pi}{2} \rho_{cu} \frac{(L_{stk} + l_{cw})}{k_a} \left(\frac{K_s}{k_w} \right)^2 \quad (25)$$

where k_{f_cond} is the copper slot fill factor excluding the slot cooling channel, k_{f_cb} is the cooling channel fill factor, and h_{s-ws} is the slot height over the slot width, and $R_{th,s}$ can be evaluated as follows:

$$R_{th,i} = \left(\frac{s_{is}}{\lambda_{is}} + \frac{1}{\alpha_s} \right) \frac{1}{S_N} \quad (26)$$

where S_{is} is the thickness of the insulation, and λ_{is} is the equivalent insulation thermal conductivity, which may be described as follows:

$$\lambda_{is} = \frac{\sum_1^n s_{is-n}}{\sum_1^n \left[\frac{s_{is-n}}{\lambda_{is-n}} \right]} \quad (27)$$

where $n = 1, 2,$ and $3,$ s_{is-1} is the thickness of the winding insulation; s_{is-2} is the slot linear insulation; and s_{is-3} is the impregnating varnish insulation. $\lambda_{is-1}, \lambda_{is-2},$ and λ_{is-3} are the thermal conductivity of the respective insulations. α_s is the heat transfer coefficient in the slots, and S_N is the total contact surface between the copper and the cooling channels and can be written again as a function of the aspect ratios as follow:

$$S_N = 2h_s l_{stk} Q = 2\pi h_{s-ws} \frac{w_s}{h_s} D_{si} l_{stk} \quad (28)$$

and the thermal resistance $R_{th,c}$ can be evaluated as follows:

$$R_{th,c} = \frac{1}{\alpha_c S_N} \quad (29)$$

where

$$\alpha_c = \frac{N_u \lambda_c}{d_{eq}} \quad (30)$$

λ_c is the thermal conductivity of the coolant, and d_{eq} is the equivalent diameter of a rectangular channel:

$$d_{eq} = 1.3 \frac{S_{ch}^{0.625}}{0.5 \text{ perim}^{0.25}} \quad (31)$$

with

$$S_{ch} = k_f \text{ ch} \left[\left(P_s * w_{s-ps} + \frac{\pi (D_{si} + 2(h_{s-ws} * w_{s-ps}))}{Q} - w_t \right) * 0.5 (h_{s-ws} * w_{s-ps} - Tt) \right] \quad (32)$$

$$\text{perim} = (k_f \text{ cond} * w_{s-ps} + h_{s-ws} * w_{s-ps}) \frac{2\pi D_{si}}{Q} \quad (33)$$

where w_{s-ps} is the slot width over the slot pitch, and N_u is the Nusselt number in the cooling channel, and it is a dimensionless parameter to reflect the enhancement of convective heat transfer due to the flow motion and it is a function of the Reynolds number Re and Prandtl number Pr . When the Reynolds number Re of the flow in the cooling channel is less than 2300, the flow is said to be laminar, whilst when higher than 4000 the flow in the cooling channels is fully turbulent. For laminar flow, the Nusselt number N_u can be calculated from Ref. [22].

$$N_u = 3.66 + \frac{\left(0.065 \cdot \frac{Re \cdot Pr \cdot d_{eq}}{D_{si} \cdot l_{Dsi}} \right)}{1 + 0.04 \cdot \left(\frac{Re \cdot Pr \cdot d_{eq}}{D_{si} \cdot l_{Dsi}} \right)^{\frac{2}{3}}} \quad (34)$$

while for the fully turbulent flow ($4000 \leq Re$)

$$N_u = \frac{(0.023 \cdot Re^{0.8} \cdot Pr^{0.4})}{1 + \left(\frac{d_{eq}}{D_{si} \cdot l_{Dsi}} \right)^{0.7}} \quad (35)$$

Generally, the Reynolds number is used to estimate whether the flow pattern inside the cooling channel of the machine is laminar, vortex, and/or turbulent, which defined as follows [23]:

$$Re = \frac{vc d_{eq} \rho_c}{\mu_c} \quad (36)$$

where ρ_c is the coolant mass density, vc is the volumetric coolant flow rate, μ_c is the dynamic viscosity of the coolant. The Prandtl number Pr can be calculated from the following equation [23].

$$P_r = c_p \mu_c / \lambda_c \quad (37)$$

where c_p and μ_c are the coolant specific heat and dynamic viscosity, respectively. From Equations (23)–(29), the machine's current loading can be determined as follows:

$$ks = \frac{\left(\Delta t_w k_a k_w^2 D_{si} l_{Dsi} \right)}{\frac{\pi}{2} \rho_{cu} (L_{stk} + l_{ew}) (R_{th,i} + R_{th,c})} \quad (38)$$

2.3 | An electromagnetic model combined with a thermal model

Generally, for the synchronous SPM motor, the electromagnetic torque equation T_e is described as follows [24]:

$$T_e = \frac{\pi}{4} B_g k_s D_{si} L_{stk} \quad (39)$$

where D_{si} is the stator inner diameter, L_{stk} is the machine active length, B_g is the air gap flux density, k_s is the electrical loading, and k_w is the winding factor. The calculation of the winding factor k_w depends on the winding topology [24].

Considering the open circuit magnetic field B_g determined by Equation (22) and the linear electric loading ks expressed by the Equation (38), the electromagnetic torque can be further written as

$$T_e = \frac{\pi}{4} B_g \sqrt{\frac{\left(\Delta t_w k_a k_w^2 D_{si} l_{Dsi} \right)}{\frac{\pi}{2} \rho_{cu} (L_{stk} + l_{ew}) (R_{th,i} + R_{th,c})}} D_{si}^3 l_{Dsi} \quad (40)$$

where l_{Dsi} is the machine aspect ratio. Another important performance parameter of the PMSM is the back-EMF. Once the flux density in the air gap of the PMSM is evaluated by the subdomain modelling using Equation (22), the phase rms value of the back-EMF is then computed using the following equation:

$$E_{ph} = \pi \sqrt{2} f N_{ph} \varphi_0 K_w \quad (41)$$

where N_{ph} is the number of turns per phase, f is the electrical fundamental frequency, and φ_0 is the no load PM flux per pole calculated by the following equation:

$$\varphi_0 = \frac{\pi}{2p} B_g D_{si} L_{stk} \quad (42)$$

Under the condition that only q-axis current is applied to the machine and d-axis current is set to zero, the phase current I_{ph} equation can then be calculated as follows:

$$I_{ph} = \frac{\pi \sqrt{2} D_{si} ks}{6 K_w N_{ph}} \quad (43)$$

For the efficiency calculation, the dc copper losses and the iron losses are considered. The copper losses in the armature winding can be estimated by

$$P_{cu} = 3/2 R_{ph} I_{ph}^2 \quad (44)$$

where R_{ph} is the electrical phase resistance.

For the iron losses per unit mass (W/kg), the general expression is given by the following equation [25]:

$$P_{iron} = \left[K_b f B^\beta + K_f K_e f^2 B^2 \right] \quad (45)$$

where, k_b is the hysteresis constant, f is the frequency of excitation, B is the fundamental peak value of the flux density in the core and β is the Steinmetz constant, k_f is the stacking factor, and k_e is the eddy current constant. Based on the curve fitting techniques on the material data provided by the manufacturer of the laminations, the constants such as k_b , k_e , and β can be calculated [25]. The magnetic flux density in the stator core (i.e., tooth B_{st} and back iron B_{sy}) can be obtained by integrating the radial components of flux density along R_s [18].

2.4 | Mechanical model

A retaining sleeve to guarantee the rotor integrity at a maximum running speed is adopted. The rotor stresses are affected by the centrifugal force and the compressive force due to the interference fit, and the increasing temperature for the sleeve can be estimated at a radius r as follows [26]:

$$\sigma_{sleeve} = \sqrt{\sigma_{rs}^2 + \sigma_r \sigma_{\theta s} - \sigma_{\theta s}^2} \quad (46)$$

where σ_c is the circumferential stress, and σ_r is the radial stress and can be calculated as follows [25]:

$$\sigma_{rs} = \frac{3 + \nu}{8} \rho \omega^2 \left[R_{sl}^2 + R^2 m - \frac{R_{sl}^2 R_m^2}{r^2} - r^2 \right] + \frac{S_0 R_m^2}{R_{sl}^2 - R_m^2} \left(1 - \frac{R_{sl}^2}{r^2} \right) \quad (47)$$

$$\sigma_{\theta s} = \frac{\rho \omega^2}{8} \left[(3 + \nu) \left(R_{sl}^2 + R^2 m + \frac{R_{sl}^2 R_m^2}{r^2} \right) - (1 + 3\nu) r^2 \right] + \frac{S_0 R_m^2}{R_{sl}^2 - R_m^2} \left(1 + \frac{R_{sl}^2}{r^2} \right)$$

where ρ is the density of the sleeve material, ω is the speed of rotation, S_0 is the contact pressure between the sleeve, and the magnet can be determined as (48) in which δ_o is the interference fit, $E_{s,m}$ and $\nu_{s,m}$ are the Young's Modulus and Poisson's ratio for the sleeve and magnet, respectively:

$$S_0 = \frac{\delta_o + \Delta T [R_{mo} \alpha_m - R_{si} \alpha_s]}{\frac{R_m \{ R_{sl}^2 (1 + \nu_s) + R_m^2 (1 - \nu_s) \}}{E_s (R_{sl}^2 - R_m^2)} + \frac{R_m \{ R_m^2 (1 - \nu_m) + R_r^2 (1 + \nu_m) \}}{E_m (R_m^2 - R_r^2)}} \quad (48)$$

where R_{mo} is the outer radius of the magnet and includes the circumferential strain at the outer radius generated by the contact pressure. R_{si} is the inner radius of the sleeve, which takes into account the circumferential strain caused by the contact pressure at the inner radius. ΔT is the change in temperature of the rotor components, and α_m and α_s are the magnet and sleeve coefficients of thermal expansion, respectively. For the purpose of the mechanical stress calculation, Table 2 provides the material properties of the rotor magnet and the sleeve.

3 | DESIGN OF THE SPM FOR AEROSPACE EHA

The traditional method of finite element can be precise and applied to non-linear and complex geometrical problems. However, since it is relatively complicated and computationally expensive, it might not be always the best design approach especially at the preliminary design stage. Alternatively, mathematical models can give quick and sufficiently accurate results and can be more effectively employed in optimisation problems, even at a preliminary design stage.

Thus, this section describes the proposed electrical machine sizing method. The sizing problem can be formulated as an optimisation problem by finding the optimum of an objective function, subject to some constraints on its design variables and generate some distinct formulations of our design problem. The optimisation problem can therefore be defined as follows:

$$\begin{aligned} & \text{Function} && \min_x && f(x) \\ & \text{Subject to} && && B_c(x) \leq f(x) \\ & && && T(x) \leq T_{\max} \\ & && && lb \leq x \leq ub \end{aligned} \quad (49)$$

Where x is a vector of the design variables. From equations of the design problem, such as those defined in Equations (22), (38), and (40), we can introduce the design variables. Hence, the key input design variables are l_{Dsi} , k_{f_chs} , h_{s_ws} , w_{s_ps} , and v_c . In the proposed optimisation problem, the motor specifications are described in Table 3, and the fixed and output design parameters are presented in Tables 4 and 5, respectively. While

TABLE 2 Material characteristics of the rotor

Properties	Sleeve (Titanium)	Properties	Magnet (SM ₂ Co ₁₇)
Density (kg/m ³)	4400	Density (kg/m ³)	8300
Young's modulus (GPa)	110	Young's modulus (GPa)	190
Poisson's ratio	0.31	Poisson's ratio	0.24
Thermal conductivity (W/m/C)	6.7	Thermal conductivity (W/m/C)	10
Permitted stress (MPa)	550	Permitted stress (MPa)	23
Yield strength (MPa)	825	Yield strength (MPa)	35
Thermal expansion (1/°C)	8.45×10^{-6}	Thermal expansion (1/°C)	11×10^{-6}
Electrical resistivity (Ω.m)	1.78×10^{-6}	Electrical resistivity (Ω.m)	0.9×10^{-6}

the dependent design parameters are shown in Table 6. $f(x)$ is the objective function that needs to be optimised and can be defined as follows:

$$f(x) = T_{\text{error}} = [\text{abs}(T_{\text{req}} - T_e)] \quad (50)$$

where T_{req} is the required torque at the operating speed, and T_e is the calculated torque that comes directly from Equation (40).

The purpose of the objective function, which is a non-linear function of the design variables, is to minimise the error T_{error} between the calculated and the required torque, without saturating the magnetic core or exceeding the material's withstanding temperature. In order to achieve this goal, a set of design constraints on the outputs are specified. The first constraint, T_{max} , relates to thermal limitations and ensures that for any design to be considered viable, the temperature in the winding must not exceed a predetermined limit, which in this case is set at 200°C. The second constraint, $B_{c,\text{max}}$, represents the maximum acceptable flux density values in the core in order to limit both high saturation and iron losses. $B_{c,\text{max}}$ depends on the material used and has a typical value between 1.8 and 2.2 T. lb and ub are the lower and upper bounds on the design variables.

The flowchart in Figure 2 depicts the complete design and optimisation process described in this section. As can be seen in Figure 2, the sizing process consists of four main stages. The key specifications (i.e., rated power and rated speed) are specified in the first stage. The fixed geometric parameters and the material properties are then assigned in the second stage on the basis of the proposed design requirements.

Starting from a user-supplied initial points, combined with Equation (40), the electromagnetic torque is calculated at stage three. Then, in order to solve the optimisation problem, a Sequential Quadratic Programming (SQP) algorithm was

TABLE 3 Key motor specifications

Requirements	Value
P_{mec} Mechanical power [w]	Determined by the designer
ω_{rot} Rotating speed [rpm]	Determined by the designer

TABLE 4 Fixed design parameters

Requirements		Value
$2p$	Number of poles	Determined by the designer
Q	Number of slots	Determined by the designer
g	Airgap length	Determined by the designer
S_o	Slot opening width	Determined by the designer
α_{PM}	PM span electrical angle	Determined by the designer
B_r	PM residual flux density	Based on the selected material
h_{PM}	PM height	Determined by the designer
t_c	Inlet coolant temperature	Determined by the designer

TABLE 5 Output design parameters

Requirements		Value
D_{si}	Inner stator diameter	Determined by the optimisation
L_{stk}	Stack length	Determined by the optimisation

TABLE 6 Dependent design parameters

Requirements		Value
h_{bi}	Stator yoke height	Determined by $\frac{B_{ry}}{2B_{rc}} \alpha_{PM} \frac{D_{si}}{P}$
w_{se}	Outer slot width	Determined by $\pi(D_{si} + 2h_s)/Q - w_t$
w_t	Tooth width	Determined by $P_s - w_s$
P_s	Slot pitch	Determined by $\pi D_{si}/Q$
h_s	Slot height	Determined by $h_{s-ws} * w_s$
w_s	Slot width	Determined by $w_{s-ps} * P_s$

considered for the multi-objective optimisation problem, as it is an efficient method which allows to deal with constrained non-linear optimisation problems [27, 28]. This algorithm converts the standard optimisation model Equation (40) into a quadratic programming sub-problem at each iteration and guides the quest path towards the solution [29].

In the implementation of the problem, the `fmincon` solver from MATLAB is used. The `fmincon` solver attempts to find the design variables, such that the value of the objective functional T_{error} is minimised, subject to the given constraints [29]. According to the optimal design variables, the machine design parameters and output performance are determined.

4 | COMPREHENSIVE SENSITIVITY ANALYSIS

For the verification work, a detailed sensitivity analysis is presented in this section to assess the effect of the most effective design parameters on machine performance. However, as compared to the other design variables, the aspect ratio $l_{D_{si}}$, cooling channel fill factor $K_{f_{cb}}$, flow rate v_c , slot height over slot width h_{s-ws} , and slot width over slot pitch w_{s-ps} are more of concern for PMSM cooled by channels installed in stator slots.

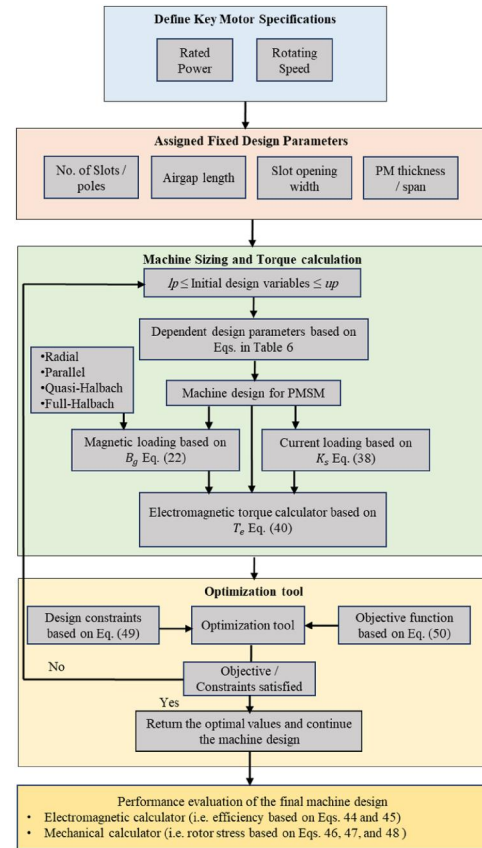
**FIGURE 2** Description of the multi-physics sizing tool.

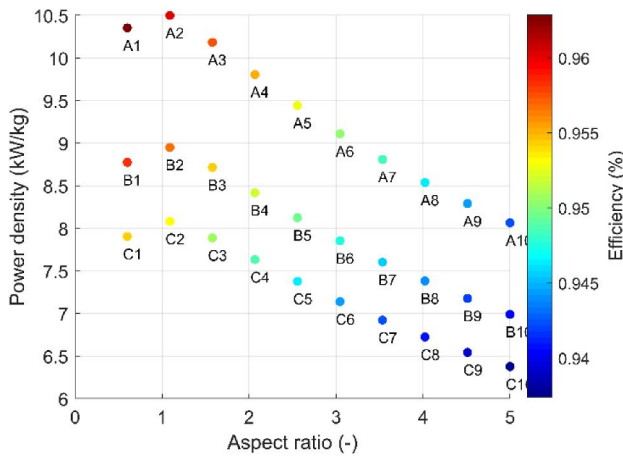
Figure 1 shows the geometric structure of the investigated PMSM to show the influence of the above-mentioned design parameters. The major parameters and corresponding variation used in the comparison are reported in Table 7. Under the condition that the machine is equipped with a slot cooling channel, the main motor specifications as well as the values of the copper fill factor, air gap thickness and magnet thickness can be determined by the specific design requirements. All solutions of the sensitivity analysis satisfy thermal and magnetic constraints with a fixed output power of 160 kW at a speed of 32,000 rpm.

The analysis has been performed, and the results are shown in Figures 3–6, which depict the different versions of feasible machine designs considered throughout the study. These machine designs are obtained according to the procedure outlined in Section 3, considering various design parameters, namely the aspect ratio $l_{D_{si}}$, cooling channel fill factor $K_{f_{cb}}$, flow rate v_c , slot height over slot width h_{s-ws} , and slot width over slot pitch w_{s-ps} . In this study, the design versions, namely $A_{(1-10)}$ to $J_{(1-10)}$, vary with the aspect ratio from 0.5 to 5 over 10 steps.

However, among the different versions of feasible machine designs considered in this analysis as shown in Figures 3–6, only a specific design with a fixed aspect ratio (e.g., 2) is reported in Tables 8–11. The aspect ratio value was selected in this analysis to allow for an appreciable comparison of different parameters of the machine designs and their

TABLE 7 Design specifications and parameters of PMSM

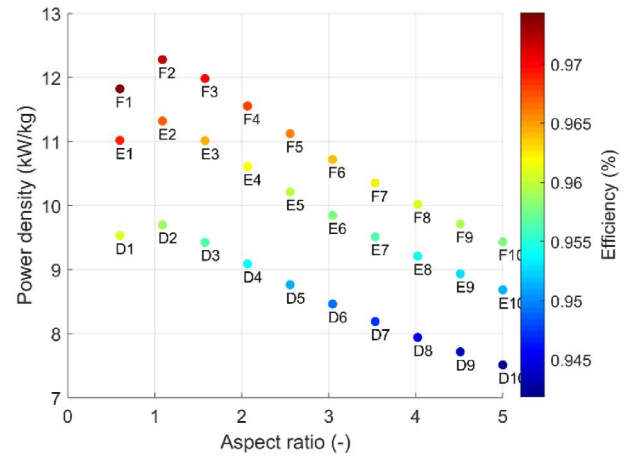
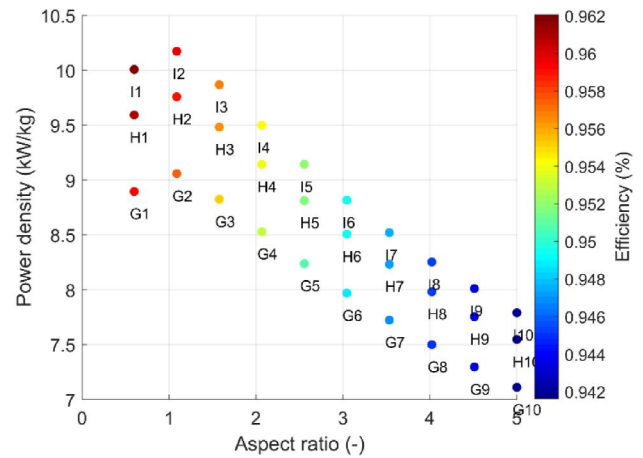
Symbol	Parameters	Motor
P_{rated}	Rated torque	160 kW
n	Rated speed	32 krpm
g	Air gap thickness	8 mm
M_T	Magnet thickness	16 mm
T_{w_max}	Maximum winding temperature	200°C
t_c	Inlet coolant temperature	120°C
L_S	Sleeve thickness	6 mm
l_{Dsi}	Machine aspect ratio	[0.5–5]
V_c	Volumetric coolant flow rate	[10–150] L/min
K_{f_cb}	Cooling channel fill factor	[0.1–0.5]
h_{s-ws}	Slot height over slot width	[1–1.5]
w_{s-ps}	Slot width over slot pitch	[0.4–0.8]

**FIGURE 3** Variation of power density and efficiency for feasible machine solutions for different aspect ratio and cooling channel fill factor with a fixed output power at 160 kW and fixed winding temperature at 200°C (Design variations A- are with $K_{f_cb} = 0.1$, B- are with $K_{f_cb} = 0.2$ and C- are with $K_{f_cb} = 0.3$).

performance. An example of this, the breakdown results are highlighted by A₍₄₎ to J₍₄₎, as shown in Tables 8–11.

Figure 3 shows the variation of power density and efficiency with the aspect ratio l_{Dsi} , and cooling channel fill factor K_{f_cb} . While, the breakdown of the results for A4, B4, and C4 are shown in Table 8. Clearly, increasing the cooling channel area in relation to the copper area (K_{f_cb}) significantly decreases the overall power density and efficiency.

This can be attributed to a decline in the copper area as a result of the cooling channel cross-section. Thus, the machine volume is consequently increased to compensate the reduction in the current density while also respecting the machine's thermal limit, allowing the maximum temperature of the winding to remain constant and the required torque to be achieved. On the other hand, as the aspect ratio increases, the

**FIGURE 4** Variation of power density and efficiency for feasible machine solutions for different aspect ratio and slot width over slot pitch with a fixed output power at 160 kW and fixed winding temperature at 200°C (Design variations D- are with $w_{s-ps} = 0.5$, E- are with $w_{s-ps} = 0.66$ and F- are with $w_{s-ps} = 0.8$).**FIGURE 5** Variation of power density and efficiency for feasible machine solutions for different aspect ratio and slot height over slot width with a fixed output power at 160 kW and fixed winding temperature at 200°C (Design variations G- are with $h_{s-ws} = 1$, H- are with $h_{s-ws} = 1.2$ and I- are with $h_{s-ws} = 1.4$).

efficiency decreases significantly because copper losses become dominant. Further, an important observation can be made when the slot width over the slot pitch w_{s-ps} is analysed and discussed, considering the data presented in Figure 4. In this figure, three differently values for w_{s-ps} are investigated. Having a high value of w_{s-ps} results in higher power density and efficiency for the possible aspect ratio combinations. An example of D4, E4, and F4 machines is given in Table 9. The increase in w_{s-ps} from 0.4 to 0.8 results in an increase in efficiency and power density of 1.46% and 26.65%, respectively. Figure 5 shows the variation of power density and efficiency with l_{Dsi} and the slot height over the slot width h_{s-w} . It can be seen that for a fixed output power, the power density increases as the h_{s-w} increases for

various values of l_{Dsi} , whereas the efficiency is nearly constant with a small variation of less than 0.4%, as highlighted by the designs G4, H4, and I4 shown in the breakdown of

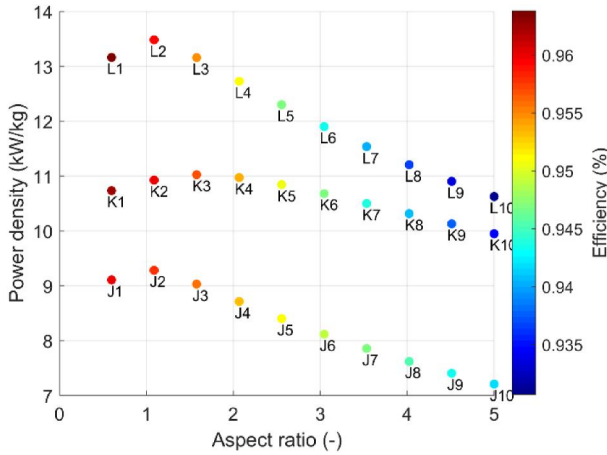


FIGURE 6 Variation of power density and efficiency for feasible machine solutions for different aspect ratio and inlet coolant flow rate with a fixed output power at 160 kW and fixed winding temperature at 200°C (Design variations J- are with $V_c = 10$, K- are with $V_c = 50$ and L- are with $V_c = 100$).

TABLE 8 Feasible machine designs with varied l_{Dsi} and Kf_{cb}

Design version	Outer diameter (mm)	Inner diameter (mm)	Stack length (mm)	Total Mass (kg)	Power density (kW)	η (%)
A4	114.8	72.6	150.2	16.3	9.8	95.5
B4	121.5	76.6	158.4	19	8.41	95.1
C4	126.2	79.3	164	21	7.63	94.8

TABLE 9 Feasible machine designs with varied l_{Dsi} and ws_{ps}

Design version	Outer diameter (mm)	Inner diameter (mm)	Stack length (mm)	Total Mass (kg)	Power density (kW)	η (%)
D4	118	74.6	154.1	17.62	9.08	95.3
E4	117.2	68.5	141.6	15.1	10.6	96.2
F4	118.1	65	134.4	13.91	11.5	96.7

TABLE 10 Feasible machine designs with varied l_{Dsi} and h_{s-ws}

Design version	Outer diameter (mm)	Inner diameter (mm)	Stack length (mm)	Total Mass (kg)	Power density (kW)	η (%)
G4	118.46	78	161.21	18.77	8.52	95.2
H4	118.1	74.27	153.49	17.5	9.14	95.3
I4	118.41	71.86	145.52	16.85	9.49	95.4

the results in Table 10. For the range of feasible aspect ratios, higher coolant flow rates result in higher power densities, but at lower efficiency, as shown in Figure 6 and the breakdown of the results for J4, K4, and L4 in Table 11. The coolant flow rate increment increases the heat transfer coefficient, which improves the heat transfer rate from the motor. This enables more current to be supplied and the machine's volume to be reduced, which results in higher power density. However, the efficiency variation with the increase in coolant flow rate drops in the range of 1%. The mechanical stress and the sleeve safety factor for the various design variables, namely l_{Dsi} , Kf_{cb} , ws_{ps} , h_{s-ws} , and V_c are also plotted in Figure 7. In this figure, the sleeve safety factor represents the limit for achieving the highest power density with acceptable mechanical stress. It can be noticed that the machines are mechanically limited to a lower aspect ratio (i.e., less than 1.5) due to higher mechanical stress in the sleeve.

In general, the aforementioned design variables appear to be effective for the design of electrical machines intensively cooled by slot cooling channels and should be considered as preliminary design parameters due to their major influence on electromagnetic, thermal, and mechanical performance.

TABLE 11 Feasible machine designs with varied l_{Dsi} and V_c

Design version	Outer diameter (mm)	Inner diameter (mm)	Stack length (mm)	Total Mass (kg)	Power density (kW)	η (%)
J4	119.78	75.59	156.23	18.36	8.71	95.3
K4	108	68.71	142	13.51	11.84	95.2
L4	105.43	67.21	138.91	12.57	12.72	95

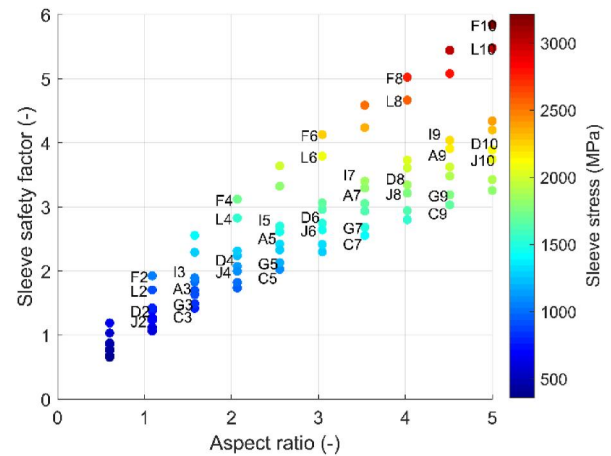


FIGURE 7 Variation of a sleeve safety factor for feasible machine solutions for different aspect ratio and cooling channel fill factor, slot width over slot pitch, slot height over slot width and coolant flow rate with a fixed output power at 160 kW and fixed winding temperature at 200°C (Design variations A- and C- are with $Kf_{cb} = 0.1$ and $Kf_{cb} = 0.3$, D- and F- are with $ws_{ps} = 0.5$ and $ws_{ps} = 0.8$, G- and I- are with $h_{s-ws} = 1$ and $h_{s-ws} = 1.4$, J- and L- are with $V_c = 10$ and $V_c = 100$).

5 | SIZING TOOL VALIDATION

In order to show the feasibility of the proposed methodology in this section, the described sizing procedure is carried out on a previously developed 9-slot/8-pole PMSM (see Figure 8) for an aerospace pump application [7]. Due to the high power density, space constraints and other challenging requirements associated with this application, a machine has been designed with a power level of 9.6 kW and a rated speed of 8700 rpm [7]. The machine is actively cooled using an oil-flooded stator cooling channel as that presented in Figure 8a. Figure 8b illustrates the prototyped machine (reference motor), and Figure 9 presents the experimental test rig. The test setup and the experimental stage of the work are described in Ref. [7].

Despite the fact that the experimental work is presented in the research done in Ref. [7], the main purpose of the present work lies in the verification of the sizing tool for SPM machines with slot oil cooling. Following the steps described in Section 3, a 9.6 kW SPM machine is designed. The demanded torque is 10.5 Nm at the rated speed of 8700 rpm. The oil inlet temperature is 90 °C, and the flow rate is limited to 4.2 L/min due to the specification of the hydraulic pumping system. Table 12 lists the input variables optimised together with the respective ranges, while Table 13 highlights the key design constraints. The optimisation results are presented in Figure 10. This figure shows the feasible design points resulting from the machine sizing tool. Among all solutions, the rational value range of the aspect ratio is reduced to the range of 1.92–2.1, contributing to determining the feasible optimal set that satisfies all the constraint conditions reported in Table 12, which means they respect the maximum phase current, DC link voltage, total machine mass, rotor moment of inertia, and envelop size. As the design constraints are satisfied,

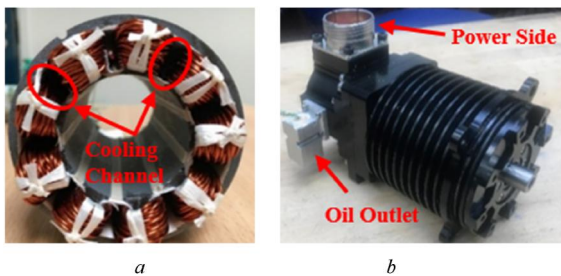


FIGURE 8 PMSM prototype (reference motor). (a) Stator core with winding and details of the cooling channel. (b) Assembled PMSM.

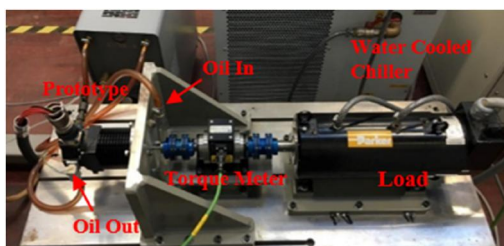


FIGURE 9 Experimental test bench.

the parameter variation of the feasible solutions is moving within a limited geometrical space (i.e., rational values range). And to select the optimal design point for this work, the solution presenting the highest efficiency and power density is marked by a red cube with an aspect ratio of 2, and the corresponding results are listed in Table 14. This table compares the analytical results of the optimal design obtained through the sizing procedure with the reference motor designed in Ref. [7]. From the table, the optimal results of the design variables fulfil the design requirements, which confirm that such sizing tool is valid for the PMSM.

Furthermore, the proposed tool's accuracy in estimating the machine's design performance has been demonstrated by comparing the optimised solution of the sizing tool with the actual performance of the developed prototype. Indeed, the analytical results are quite consistent with the measured values,

TABLE 12 Input design parameters

Input design variables	Range properties
l_{Dsi}	0.5–5
ω_{s-ps}	0.4–0.7
h_{s-ws}	1–1.5
K_{f-ch}	0.1–0.2

TABLE 13 Key motor constraints

Requirements	Value
Torque @ 8700 rpm	10.5 Nm
Dc link voltage	270 dc
Rated current	≤ 80 a
Moment of inertia	$\leq 1 \times 10^{-4}$ kg · m ²
Weight	≤ 2.5 kg
Stator outer diameter	≤ 70 mm
Machine active length	≤ 80 mm
Max. winding temperature	210 °C

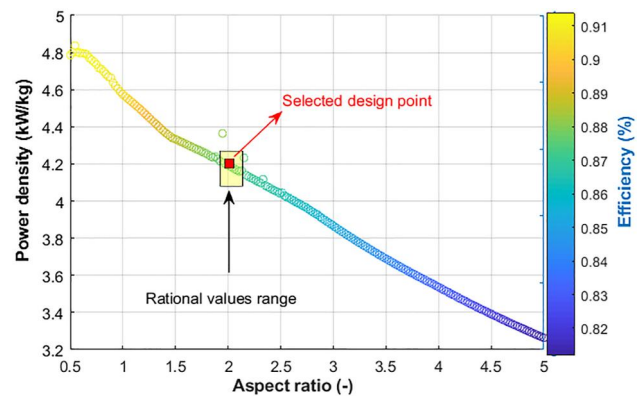


FIGURE 10 Feasible designs resulting from the machine sizing tool.

TABLE 14 Comparison of key performance as generated by the sizing tool and the developed prototype (Reference Motor) @ 10.5 Nm and 8700 rpm

Parameters	Reference motor Prototype	Designed motor	
		FEM	Analytical
Number of poles (–)	8	8	
Number of slots (–)	9	9	
DC link voltage (V)	270	270	
Maximum current (A)	80	80	
Machine aspect ratio (–)	2.13	2	
Stator outer diameter (mm)	70	67.81	
Stator inner diameter (mm)	37.45	38.22	
Stack length (mm)	80	76.45	
Slot width/slot pitch (–)	0.708	0.63	
Slot height/slot width (–)	1.379	1.23	
Channel fill factor (–)	0.23	0.3	
Mass (kg)	2.5	2.31	
Volume (L)	0.307	0.276	
Efficiency (%)	86.7	86.81	87.4
Power density (kW/kg)	3.58	4	4.15

which include additional practical manufacturing considerations. Therefore, the proposed sizing tool, which allows for the search of a wide range of design parameters, has proved to be an effective method for designing high performance and high-power-density machines intensively cooled by slot channels.

6 | CONCLUSION

This paper introduced and outlined the approach used for developing a quick and accurate sizing tool that can be used to investigate and compare a wide range of various combinations of electrical machines in the early stages of machine design and system integration for aviation electrification. An analytical sizing approach combined with a sub-domain model and the SQP algorithm has been proposed in this study to efficiently perform the preliminary design among the design objectives of an SPM machine that is actively cooled by oil channels placed in the stator slots.

For the investigated scenario, it was demonstrated that high levels of kW/kg are achievable by combining the intensive cooling strategy with integrated optimisation of machine dimensions parameters, specifically cooling channel dimensions and aspect ratio. As a vessel to verify the validity of the proposed sizing tool, a previously developed PMSM [28] for an aerospace application is considered in this work. The experimental results are consistent with the analytical prediction.

Although the methodology is aimed at maximising power density, an analogous sizing approach may also be easily implemented to optimise other objectives and improve PMSM's

capabilities for specific targets. Since the computation time is fast with acceptable accuracy, the technique described in this work is intended to be a valuable tool for electrical machine designers throughout the design stage, allowing them to make system-level actions. However, a slight difference caused by ignoring the stator core saturation and machine complex geometry remains a downside of this approach and hence remains a challenge to be solved.

AUTHOR CONTRIBUTIONS

Ahmed Tameemi: Writing – review & editing. **Michele Degano:** Writing – review & editing. **Mukhammed Murataliyev:** Writing – review & editing. **Mauro Di Nardo:** Writing – review & editing. **Giorgio Valente:** Writing – review & editing. **David Gerada:** Writing – review & editing. **Zeyuan Xu:** Writing – review & editing. **Chris Gerada:** Writing – review & editing.



CONFLICT OF INTEREST

The authors state that there is no conflict of interest in publishing this manuscript.

DATA AVAILABILITY STATEMENT

Research data are not shared.

ORCID

Ahmed Tameemi  <https://orcid.org/0000-0003-0306-0837>
Mauro Di Nardo  <https://orcid.org/0000-0003-0137-4920>

REFERENCES

- Dorn-Gomba, A.L., et al.: Power electronic converters in electric aircraft: current status, challenges, and emerging technologies. *IEEE Trans. Transp. Electrification* 6(4), 1648–1664 (2020). <https://doi.org/10.1109/tte.2020.3006045>
- Madonna, V., Giangrande, P., Galea, M.: Electrical power generation in aircraft: review, challenges, and opportunities. *IEEE Trans. Transp. Electrification* 4(3), 646–659 (2018). <https://doi.org/10.1109/tte.2018.2834142>
- Wheeler, P., Bozhko, S.: The more electric aircraft: technology and challenges. *IEEE Electrification Mag.* 2(4), 6–12 (2014). <https://doi.org/10.1109/mele.2014.2360720>
- Golovanov, D., et al.: 4-MW class high-power-density generator for future hybrid-electric aircraft. *IEEE Trans. Transp. Electrification* 7(4), 2952–2964 (2021). <https://doi.org/10.1109/tte.2021.3068928>
- Khatre, M.: Reduced DC-link capacitor drives for more-electric aircraft applications (2010)
- Alle, N., et al.: Review on electro hydrostatic actuator for flight control. *Int. J. Fluid Power* 17(2), 125–145 (2016). <https://doi.org/10.1080/14399776.2016.1169743>
- Al-Timimy, A., et al.: Design and losses analysis of a high power density machine for flooded pump applications. *IEEE Trans. Ind. Appl.* 54(4), 3260–3270 (2018). <https://doi.org/10.1109/tia.2018.2821623>
- Ponomarev, P., et al.: Design of integrated electro-hydraulic power unit for hybrid mobile working machines. In: *Proceedings of the 2011 14th European Conference on Power Electronics and Applications*, pp. 1–10 (2011)
- Powell, D.J., Atallah, K., Jewell, G.: Thermal modeling of flooded rotor electrical machines for electro-hydrostatic actuators. In: *Electric Machines & Drives Conference, 2007. IEMDC'07. IEEE International*, pp. 1632–1637 (2007)
- Lindh, P.M., et al.: Direct liquid cooling in low-power electrical machines: proof-of-concept. *IEEE Trans. Energy Convers.* 31(4), 1257–1266 (2016). <https://doi.org/10.1109/tec.2016.2597059>

11. Lindh, P., et al.: Direct liquid cooling method verified with a permanent-magnet traction motor in a bus. *IEEE Trans. Ind. Appl.* 55(4), 4183–4191 (2019). <https://doi.org/10.1109/tia.2019.2908801>
12. Schiefer, M., Doppelbauer, M.: Indirect slot cooling for high-power-density machines with concentrated winding. In: 2015 IEEE International Electric Machines & Drives Conference (IEMDC), pp. 1820–1825. Coeur d'Alene, ID (2015)
13. Reinap, A., et al.: Direct conductor cooling in concentrated windings. In: 2018 XIII International Conference on Electrical Machines (ICEM), pp. 2654–2660. Alexandroupoli (2018)
14. Petrov, I., et al.: Investigation of a direct liquid cooling system in a permanent magnet synchronous machine. *IEEE Trans. Energy Convers.* 35(2), 808–817 (2020). <https://doi.org/10.1109/tec.2019.2952431>
15. Acquaviva, A., Skoog, S., Thiringer, T.: Design and verification of in-slot oil-cooled tooth coil winding PM machine for traction application. *IEEE Trans. Ind. Electron.* 68(5), 3719–3727 (2021). <https://doi.org/10.1109/tie.2020.2985009>
16. Acquaviva, A., et al.: Computationally efficient modeling of electrical machines with cooling jacket. *IEEE Trans. Transp. Electrification* 5(3), 618–629 (2019). <https://doi.org/10.1109/tte.2019.2936122>
17. Tiang, T.L., et al.: A comprehensive analytical subdomain model and its field solutions for surface-mounted permanent magnet machines. *IEEE Trans. Magn.* 51(4), 1–14 (2015). <https://doi.org/10.1109/tmag.2014.2361484>
18. Min, S.G., Sarioglu, B.: Fast and systematic design optimization of surface-mounted PM machines using advanced analytical models and subharmonic elimination methods. *IEEE Trans. Magn.* 55(1), 1–16 (2019). Art no. 8100216. <https://doi.org/10.1109/tmag.2018.2877403>
19. Rezal, M., Ishak, D.: Performance evaluation of multi-phase permanent magnet synchronous motor based on different winding configurations and magnetization patterns. *Int. J. Power Electron. Drive Syst.* 10(3), 1197 (2019). <https://doi.org/10.11591/ijpeds.v10.i3.pp1197-1206>
20. Shen, Y., Zhu, Z.: General analytical model for calculating electromagnetic performance of permanent magnet brushless machines having segmented Halbach array. *IET Electr. Syst. Transp.* 3(3), 57–66 (2013). <https://doi.org/10.1049/iet-est.2012.0055>
21. Wu, L.J., et al.: Subdomain model for predicting armature reaction field of surface-mounted permanent-magnet machines accounting for tooth-tips. *IEEE Trans. Magn.* 47(4), 812–822 (2011). <https://doi.org/10.1109/tmag.2011.2104969>
22. Semiday, S.A., Mayor, J.R.: Experimentation of an electric machine technology demonstrator incorporating direct winding heat exchangers. *IEEE Trans. Ind. Electron.* 61(5), 71–78 (2014). <https://doi.org/10.1109/tie.2014.2303779>
23. Nategh, S., et al.: Thermal modeling of directly cooled electric machines using lumped parameter and limited CFD analysis. *IEEE Trans. Energy Convers.* 28(4), 979–990 (2013). <https://doi.org/10.1109/tec.2013.2283089>
24. Lipo, T.A.: *Introduction to AC Machine Design*, 2nd ed. University of Wisconsin Press, Madison (2004)
25. Zhu, Z., et al.: Evaluation of iron loss models in electrical machines. *IEEE Trans. Ind. Appl.* 55(2), 1461–1472 (2019). <https://doi.org/10.1109/tia.2018.2880674>
26. Damiano, A., et al.: Modelling and design of PM retention sleeves for high-speed PM synchronous machines. In: *Electric Drives Production Conference (EDPC), 2016 6th International*, pp. 118–125 (2016)
27. Zhu, X., et al.: Multiobjective optimization design of a double-rotor flux-switching permanent magnet machine considering multimode operation. *IEEE Trans. Ind.* 66(1), 641–653 (2019). <https://doi.org/10.1109/tie.2018.2818643>
28. Zhu, X., et al.: Comprehensive sensitivity analysis and multiobjective optimization research of permanent magnet flux-intensifying motors. *IEEE Trans. Ind.* 66(4), 2613–2627 (2019). <https://doi.org/10.1109/tie.2018.2849961>
29. Dominic, A., Schullerus, G., Winter, M.: Dynamic energy efficient control of induction machines using anticipative flux templates. *Applied Sciences* 11(6), 2878 (2021). <https://doi.org/10.3390/app11062878>

How to cite this article: Tameemi, A., et al.: Design procedure and optimisation methodology of permanent magnet synchronous machines with direct slot cooling for aviation electrification. *IET Electr. Power Appl.* 17(4), 522–534 (2023). <https://doi.org/10.1049/elp2.12281>